Physics in Medicine & Biology

IPEM Institute of Physics and Engineering in Medicine

OPEN ACCESS

RECEIVED
18 June 2021

REVISED
22 October 2021

ACCEPTED FOR PUBLICATION
30 November 2021

PUBLISHED
23 December 2021

PAPER

Gradient coil and radiofrequency induced heating of orthopaedic implants in MRI: influencing factors

J Wooldridge[1,*], **A Arduino**[2], **L Zilberti**[2], **U Zanovello**[2], **M Chiampi**[2], **V Clementi**[3] and **O Bottauscio**[2]

[1] National Physical Laboratory, Hampton Road, Teddington, Middlesex, TW11 0LW, United Kingdom
[2] Istituto Nazionale di Ricerca Metrologica, Str. delle Cacce, 91, I-10135 Torino TO, Italy
[3] IRCCS Istituto Ortopedico Rizzoli, Laboratorio di Tecnologia Medica, Via di Barbiano 1/10, I-40136 Bologna, Italy
[*] Author to whom any correspondence should be addressed.

E-mail: jenny.wooldridge@npl.co.uk and o.bottauscio@inrim.it

Keywords: MRI, implant heating, finite element modelling

Abstract

Patients with implanted orthopaedic devices represent a growing number of subjects undergoing magnetic resonance imaging (MRI) scans each year. MRI safety labelling is required for all implants under the EU Medical Device Regulations to ensure regulatory compliance, with each device assessed through standardised testing procedures. In this paper, we employ parametric studies to assess a range of clinically relevant factors that cause tissue heating, performing simulations with both radio-frequency (RF) and gradient coil (GC) switching fields, the latter of which is often overlooked in the literature. A series of 'worst-case' scenarios for both types of excitation field is discussed. In the case of GC fields, large volume implants and large plate areas with the field orientated perpendicular to the plane cause the highest heating levels, along with sequences with high rates of field switching. Implant heating from RF fields is driven primarily from the 'antenna effect', with thin, linear implants of resonant length resulting in the highest temperature rises. In this work, we show that simplifications may be made to the field sequence and in some cases the device geometry without significantly compromising the accuracy of the simulation results, enabling the possibility for generic estimates of the implant heating for orthopaedic device manufacturers and opportunities to simplify the safety compliance process.

1. Introduction

Orthopaedic implants represented a €9Bn market in the EU in 2020 (Market Data Forecast Ltd 2020). Approximately 50 million EU citizens carry a medical implant (Lidgren *et al* 2020) and a majority of these will need a magnetic resonance imaging (MRI) scan during the lifetime of their device (Bhuva *et al* 2020). However, the issue of implant heating from switched magnetic field gradients and radio frequency (RF) fields represents a unique safety hazard for these patients. It is vital for both patient safety and the success of a medical implant on the market that implant manufacturers can demonstrate safety compliance in an MRI environment (Schaefers and Melzer 2006, Stijnman *et al* 2020).

There are two current safety standards applicable to implant device heating in MRI scans: ASTM F2182 (ASTM F2182—19e2, 2019) and ISO/IEC TS 10 974 (ISO/TS 10974:2018, 2018), the former being related to RF heating of passive implants, while the latter being restricted to active implants in 1.5T scanners. The application of those standards is costly and lengthy: a mistake can be damaging for both patient and manufacturer. While large producers of high-end active implantable medical devices are facing technological challenges to demonstrate MRI compatibility, small and medium-sized enterprises manufacturing passive medical implants are overburdened by the necessity to demonstrate MRI safety for each new size and shape of a particular device, therefore limiting their innovation potential.

This paper aims to evaluate the implant-related factors affecting tissue heating for both RF and gradient coil (GC) heating, providing commentary on the relevant factors involved in heating in orthopaedic implants. This understanding helps in identifying a subset of worst-case configurations for evaluation, potentially allowing for

reduced numbers of simulations and measurements required to demonstrate regulatory compliance. This analysis is conducted in a complementary way with respect to the procedures proposed for searching for the worst case configuration in Liu *et al* (2013), Zheng *et al* (2020a, 2020b) and can help in the identification of the fundamental parameters in artificial neural network modelling, as proposed in Zheng *et al* (2020a, 2020b).

2. Methods

2.1. Gradient coil heating models

The thermal heating due to the GC field was evaluated by computing (a) the distribution of the power density within the implant consequent to the interaction between the magnetic field and the metallic object and (b) the subsequent heating of the metallic object and thermal diffusion towards a rectangular gelled saline phantom of size 0.65 m $\times$ 0.42 m $\times$ 0.09 m and material properties in accordance with ASTM F2182 (ASTM F2182—19e2, 2019). The implant and the surrounding phantom were discretized into homogeneous cubic voxels of given electrical and thermal properties. The size of the voxels ranges from 0.25 mm to 1 mm depending on the geometrical details of the simulated implant. The size guarantees stable results and is always significantly lower than the penetration depth of the gradient field in the metallic implants for all the simulated pulse sequences. For step (a), the electromagnetic problem was conveniently limited to the region of the metallic objects, assuming that induced currents and related power deposition are confined within the implant at the low frequencies of the GC field. In order to account for the complex time evolution of realistic sequences, the approach proposed and validated in (Arduino *et al* 2019) was adopted. The time waveforms of the magnetic field signals were decomposed into truncated Fourier series. For each signal the related electromagnetic problem, which involves the field reaction caused by induced currents, was solved in the frequency domain using the hybrid Finite Element/Boundary Element solver described in (Bottauscio *et al* 2015) and (Zilberti *et al* 2015). Finally, the induced currents and the powers deposited in each voxel were evaluated.

For step (b), the thermal problem generated by the power deposition in the metal was solved in the whole domain (metallic object and phantom) using Pennes' bioheat equation in terms of the temperature elevation ϑ_t after time t with respect to the temperature at rest T_0. Robin boundary conditions were set on the external surface of the phantom to account for the heat exchange with the ambient atmosphere. The bioheat equation was numerically solved by a finite difference method (FDM) using a Douglas-Gunn (DG) time split scheme, which allows for an efficient parallel implementation on graphics processing units (GPUs) (Arduino *et al* 2017).

For all the simulations reported in the paper, the GC field was assumed to be spatially uniform in the region of the implant. This assumption makes the results more general, freeing them from the complex spatial distribution of GC fields, which are specific to the scanner model (Arduino *et al* 2019). Thanks to the linearity of the electromagnetic and thermal problems, the results can be adapted to any GC field amplitude B_{GC}, by rescaling the total deposited power and the peak temperature elevation by the factor B_{GC}^2.

Because of the different sizes, numbers of harmonics and conditioning numbers, the computational time varied between different problems, but it was always of the order of some hours.

2.2. RF heating models

RF heating simulations were constructed using Comsol Multiphysics v5.5 (Comsol, 2020); model results have been validated against analytical solutions for simple implant geometries (Zilberti *et al* 2020), and against measurement results by other authors (Ruoff *et al* 2012). A 16 rung birdcage coil was modelled with a geometry to match those of body coils in typical commercial scanners (birdcage radius of 0.3 m, length of 0.6 m, high-pass design). An RF shield (of radius 0.4 m and length 0.7 m) is placed around the birdcage coil (Giovannetti *et al* 2002). The entire system is enclosed within an air sphere of radius 1.5 m, with the phantom located centrally within the coil. Implants are placed within the phantom centred on the isocentre plane of the coil, located close to the edge of the phantom within the highest intensity and most uniform section of the electric field (see appendix A).

The coil and shield are both modelled within Comsol as perfect electrical conductors. The coil is excited at the mid-point of each rung with sinusoidal inputs of 63.9 MHz and 127.7 MHz (a stationary magnetic flux density B_0 of 1.5 T and 3 T respectively), varying in phase from 0 rad to 2π rad around the circumference of the coil. A capacitor is placed at the top and bottom of each rung, and a series of parametric sweeps in capacitance were performed to tune the coil to the desired mode 1 resonance frequency (Giovannetti *et al* 2002) for each B_0 field. The outermost sphere in the geometry is defined as an absorbing boundary to prevent any reflections into the modelling domain. Finally, given the skin depth of the metallic implants is in the range 30–80 μm for the materials and frequencies considered in this study, the internal parts of the implant were not calculated within the electromagnetic part of the simulation; rather the surface of the implant was modelled using an impedance boundary condition (Zilberti *et al* 2020).

Table 1. Characteristics of the trapezoidal sequences considered in the analysis. The amplitude of B_{GC} is set to 23 mT m^{-1}.

Trapezoidal sequence	$\frac{t_s}{2}$(ms)	t_d(ms)	Fundamental frequency f(Hz)	$I_s(T/(\text{ms}))$
SEQ_1	0.147	0.32	815	110.6
SEQ_2	0.500	0.32	379	40.9
SEQ_3	0.147	1.00	386	76.2
SEQ_4	0.100	0.32	962	145.8
SEQ_5	0.300	0.32	543	63.2
SEQ_6	0.147	0.00	1695	159.9
SEQ_7	0.147	3.00	152	47.8
SEQ_8	0.100	0.25	1111	156.7
SEQ_9	0.500	3.00	125	27.5
SEQ_{10}	3.000	4.00	50	13.5

Within the thermal simulations, an initial temperature of 294.15 K was set for all the geometric domains and, following the whole body Specific Absorption Rate (SAR) measurement protocol in ASTM F2182 (ASTM F2182—19e2, 2019), the outer boundaries of the phantom were defined as thermally insulated. The gelled saline within the phantom is assumed to be a solid, with no convective currents present. The amplitude of the voltage applied to the coil was adjusted in both B_0 models to achieve an average temperature rise in the phantom (with no implant) after 900 s, equivalent to a whole body SAR of 2 W kg^{-1}

$$\text{SAR} = c_P \frac{\vartheta_t}{t}, \tag{1}$$

where c_P is the specific heat capacity of the phantom, ϑ_t the temperature rise in kelvin and t the time in seconds. Post processing of the simulations established this calculation for average SAR in the phantom to be numerically equal (within 3 ppm) to the SAR calculated from the electric field

$$\text{SAR} = \frac{\sigma |\boldsymbol{E}|^2}{2 m_d}, \tag{2}$$

where σ is the electrical conductivity, $\boldsymbol{E}$ is the electric field and m_d is the mass density.

The RF induced heating around the implants is modelled with the coupled electromagnetics and transient heat transfer modules in Comsol. The propagation of the RF fields generated by the birdcage coil is described by

$$\nabla \times \mu_r^{-1}(\nabla \times \boldsymbol{E}) - k_0^2 \left(\epsilon_r - \frac{j\sigma}{\omega \epsilon_0} \right) \boldsymbol{E} = 0, \tag{3}$$

where μ_r is the relative magnetic permeability, k_0 the wave number of free space, ϵ_r the relative permittivity, ϵ_0 the permittivity of free space and ω the angular frequency.

The heat flow in solids is derived from the heat equation with Fourier's law

$$m_d c \frac{\partial \vartheta_t}{\partial t} = \nabla \cdot (\kappa \nabla \vartheta_t) + Q, \tag{4}$$

where κ is the thermal conductivity and Q the heat source. The heat source in this case is generated by the SAR from the electromagnetic field, and from Joule heating arising within the implant, which represents the coupled physics within the model.

Within the simulation geometry, the minimum mesh element size employed was dependent on the particular implant under investigation, however was set to 0.1 mm for the smallest diameter cylinders and thinnest plates. Mesh convergence studies were completed on the empty phantom to achieve stable results for the incident B_{RF} field. The total number of elements in the simulations ranged from 1.4×10^5 to 1.3×10^6. Each simulation took approximately 1 h to complete, however the parametric studies were carried out in parallel on an high-performance computing facility reducing the overall simulation times.

2.3. Prostheses and scan sequences

Within the subsequent sections, a range of simplified implant geometries and common orthopaedic implants has been modelled, along with investigations into the effects of different GC sequences and a variety of materials properties (both within the implant and the phantom). The intention is to cover as broad a range of clinical situations as reasonably possible, and to investigate how well predictions made from generic shapes can be applied to realistic implant models. The electromagnetic and thermal properties of the materials simulated in this study are presented in appendix B.

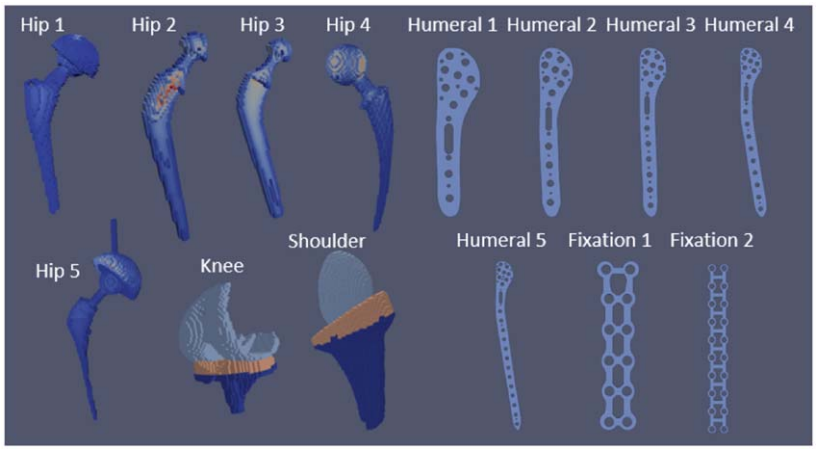

Figure 1. Orthopaedic implants considered in this study (not to scale).

Table 2. Characteristics of the clinical sequences considered in the analysis.

Clinical sequence	Number of signals	Fundamental frequency f (Hz)	$I_s(T/(\text{ms}))$
EPI (only frequency encoding)	1	961	11.8
3D-FISP	3	156	78.7
3D-FSPGR	3	86	71.1
ax T1 HR (fat sat)	3	17	40.9
ax T2 (fat sat) (FRFSE)	3	0.86	54.8
TrueFisp bSSFP	3	256	160.2
slab ax 3D mdc (3D—FSPGR)	3	68.5	58.4

Since the time waveforms of the GC sequences are mainly composed of trapezoidal signals, a set of trapezoidal waveforms of the B_{GC} field, with variable rise time $t_s/2$ and flat level duration t_d, were adopted in the analysis. The results given by these waveforms, denoted by the symbols SEQ_1 to SEQ_{10}, were also compared with those provided by actual clinical sequences. An index of thermal stress I_s, which neglects the skin effect, was associated with each waveform, computed as

$$I_s = \sqrt{\frac{1}{T}\int_0^T \left(\frac{dG}{dt}\right)^2 dt}, \tag{5}$$

where G is the magnetic field gradient, T is the period of the trapezoidal waveform having fundamental frequency $f = 1/T$, and the field amplitude B_{GC} is set to 23 mT m^{-1}. The characteristics of the considered trapezoidal signals, including their stress index, are reported in tables 1 and 2 together with the characteristics of some clinical sequences considered in the further analysis. For the clinical sequences, the three signals associated with the GCs were superposed assuming that all the GCs generate the same homogeneous field within the implant; hence, the stress index was computed for the signal resulting from their sum.

The GC analysis was performed considering seven large orthopaedic implants (five models of hips, one model of knee and one model of shoulder), four classes of smaller plate orthopaedic implants (humeral plates of length 90 mm to 230 mm and grid fixation plates of length 45 mm to 86 mm) and six screws, modelled as cylinders, whose diameter and axial length range from 2 mm to 7 mm and from 4 mm to 140 mm, respectively. The large and small orthopaedic implants under analysis are shown in figure 1. RF simulations were performed on the smaller orthopaedic implants and cylinders. These simulations did not include the large implants; there are many published studies describing RF heating in orthopaedic prostheses already (Stenschke *et al* 2007, Powell *et al* 2012, Kabil *et al* 2016, Mosher *et al* 2018) and, as will be described in the sections below, implant mass is more of an issue for GC heating compared with RF heating.

In addition, the investigations were extended to spheroids (GC only) and generic rectangular plates (both GC and RF simulations). The spheroids are fully defined by the semi-axis L_s along the z-axis and the radius R_s in

the *xy*-plane, the cylinders similarly by the length L_c along the *z*-axis and radius R_c in the *xy*-plane, and the plates by the dimensions in the *xy*-plane and the thickness. For spheroids, parameters R_s and L_s were varied in the range from 2 mm to 20 mm and from 2 mm to 90 mm, respectively, generating in total 40 spheroids, whose dimensions cover most of the sizes of realistic prostheses, from small screws to large knee implants. With the cylinders, R_c and L_c were varied over the range from 1 mm to 10 mm and 10 mm to 300 mm, respectively, resulting in a data set of 600 points for both B_0 fields. The predominant effect in RF heating relates to the antenna effect (Winter *et al* 2020) and so the parameter values covered, whilst extending outside the range considered for 'small' implants, were designed to cover the half-wavelength range for the RF field within the phantom. For generic plates the sizes were varied from 20 mm to 250 mm and thickness from 1 mm to 3.5 mm.

3. Results

3.1. Parameters affecting GC power deposition and heating

The power deposition *P* in a metallic implant is determined by the amplitude of the eddy currents flowing within the object, which in turn is strictly related, besides the object size, to its average cross section perpendicular to the direction of the applied magnetic field. In approximately 2D objects, i.e. objects where one dimension is much smaller than the others, the strongest coupling between field and object occurs when the field is perpendicular to the implant surface. On the contrary, the definition of the most severe condition is not straightforward for complex 3D objects, so that different orientations of the field with respect to the object must be investigated. For this reason, in the subsequent analysis the behaviour of approximately 2D implants will be discussed separately from their 3D counterparts. Most of the orthopaedic plates are classified as 2D objects, whereas orthopaedic implants such as hip, shoulder and knee prostheses belong to the 3D category, as well as screws, despite their small size.

Power deposition is also affected by the GC field amplitude and the harmonic content of the GC signals, which is accounted for in the stress index I_s, defined in section 2.3, as well as from the local value of the GC field and the electrical conductivity of the implant. All these contributions were separately analysed and *P* is modelled as

$$P = k_p B_G^2 f(I_s) \beta, \tag{6}$$

where k_p is a coefficient related to the implant characteristics (size/shape and electrical conductivity of the material), B_G is a coefficient related to the GC field amplitude in the considered position within the scanner (it is the amplitude of the local GC magnetic flux density corresponding to a gradient field equal to 1 T m^{-1}), $f(I_s)$ is a coefficient which depends on the GC sequence characteristics (summarised in the stress index I_s), and $\beta \leqslant 1$ is a factor which accounts for the relative orientation of the GC field with respect to the implant.

The temperature increases ϑ_{360} and ϑ_{900} induced within the implant and the surrounding tissues due to the power deposited by the GC field were evaluated after 360 s and 900 s of exposure, respectively. Both the considered temperature increases can be written as

$$\vartheta_t = g(P, \ \Xi), \tag{7}$$

where Ξ accounts for the heat exchange with the phantom (including thermal properties of the phantom and external surface of the object).

3.1.1. Sequence parameter: effect of the stress index

The characteristics of the time waveform of the GC signals determine the number and amplitude of the harmonic components of the magnetic field and, consequently, the amplitude and evolution of the eddy currents induced within the metallic object. The deposited power *P* obtained with ten simplified trapezoidal waveforms, having various rising time and dwell time, was computed for a selection of large and small orthopaedic implants.

The adopted parameter to describe the sequences was the stress index I_s defined in section 2.3, whose values range from about 13 $T/$(ms) to about 160 $T/$(ms), covering large classes of clinical sequences (see table 2). Panel A of figure 2 shows the total power *P* deposited into the large orthopaedic implants versus the parameter I_s, comparing the results obtained with trapezoidal waveforms and a set of clinical sequences. For each implant, the maximum power with respect to the reciprocal orientation of the field and the implant is reported in the plot. Power *P* scales with a good approximation with the square of I_s as evident from fitting polynomials to the data (degree 2 was found to be satisfactory) reported in the figure (dashed lines), such that $f(I_s)$ can be stated as $f(I_s) = I_s^2$ in equation (6). In the case of larger implants, higher electrical conducitivty (see also section 3.1.4) or in the case of signals having a higher harmonic contents, skin effects can arise within the metal; this effect will give rise to a dependence of power *P* versus I_s having a slightly lower exponent. For the same trapezoidal

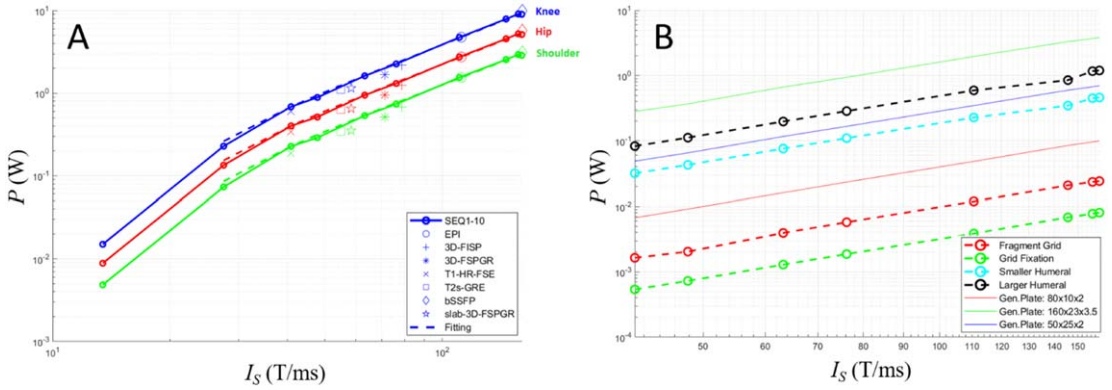

Figure 2. Influence of parameter I_s on power deposition for large orthopaedic implants (panel A) and 2D implants (panel B). For each object, the maximum power with respect to the relative orientation of the field and the object is reported. For the large implants, the results obtained with trapezoidal waveforms are compared with those obtained with some clinical sequences.

sequences, simulations were performed both on large and small orthopaedic implants, showing a similar trend for P.

Panel B of figure 2 shows the results obtained with 2D implants, comparing small orthopaedic implants with generic plates of different size. In this case, the worst condition of the field perpendicular to the implant surface was considered. Again, a square dependence of P on I_s is found (see curve fitting for the generic plate of size 160 mm × 23 mm × 3.5 mm), independently from the geometrical characteristics (shape, size, presence of holes).

This analysis shows how the parameter I_s provides a good quantitative indicator, able to correlate the characteristics of the GC field time waveform with the power deposition. This observation suggests the possibility of using simplified sequences in laboratory tests instead of complex sequence waveforms to reproduce similar thermal stresses.

3.1.2. 3D objects: effect of size and field direction

All the considered objects belonging to the three categories of devices (large orthopaedic implants, screws, spheroids) were analysed, evaluating P, ϑ_{360} and ϑ_{900} for a given GC signal (SEQ_8 from section 2.3). The devices were assumed to be made of CoCrMo-alloy and inserted within a phantom having the thermal properties of the ASTM gel. For the spheroid, the orientation of the applied field was varied along five directions with respect to the z-axis, taking advantage of the rotational symmetry of the object. For the hip, shoulder and knee implants, 13 orientations were explored covering most of the relative orientations. For the screws, only the field directions parallel and normal to the screw axis were analysed. For each implant, the deposited power and the temperature increase were evaluated considering all the field orientations related to the device category and the maximum computed values (P_{max}, ϑ_{360}, ϑ_{900}) were associated with the implant under analysis. The dependence of the power deposition on the GC field orientation is presented in figure 3, where results refer to the more complex 3D large implants and their components; in particular, the variability is larger for the knee and the 'hip5' implants, whereas it is limited for devices with a simpler structure, like 'hip4'. Figure 4 collects all the results obtained for the family of considered spheroids, the realistic large orthopaedic implants and the screws; for each implant the maximum power with respect to field orientation is considered and the corresponding parameter k_p is shown. The volume is found to be a crucial parameter affecting both the power deposition and the temperature increase. In particular, figure 4 shows how the values of k_p are well correlated with the implant volume. Indeed, all k_p values are located within a narrow strip along a straight line in logarithmic scale, regardless of the device category. The correlation between the results obtained with spheroids and actual implants (including screws) gives at least the possibility of maximising the value of the deposited power in devices with a complex geometry by using simplified shapes having a similar volume.

3.1.3. 2D objects: effect of cross section

The analysis of 2D objects was carried out only for the worst condition, assuming the GC field to be perpendicular to the object plane (xy-plane) and evaluating the corresponding value of the total power P. The results can be generalised to any value of the angle α between the GC field and the unit vector perpendicular to the object plane, rescaling P by the factor $\cos^2 \alpha$.

The power deposited in the 2D objects can be reasonably assumed to have a linear dependence with the thickness d, so that the ratio between coefficient k_p and thickness was analysed. Figure 5 shows how this

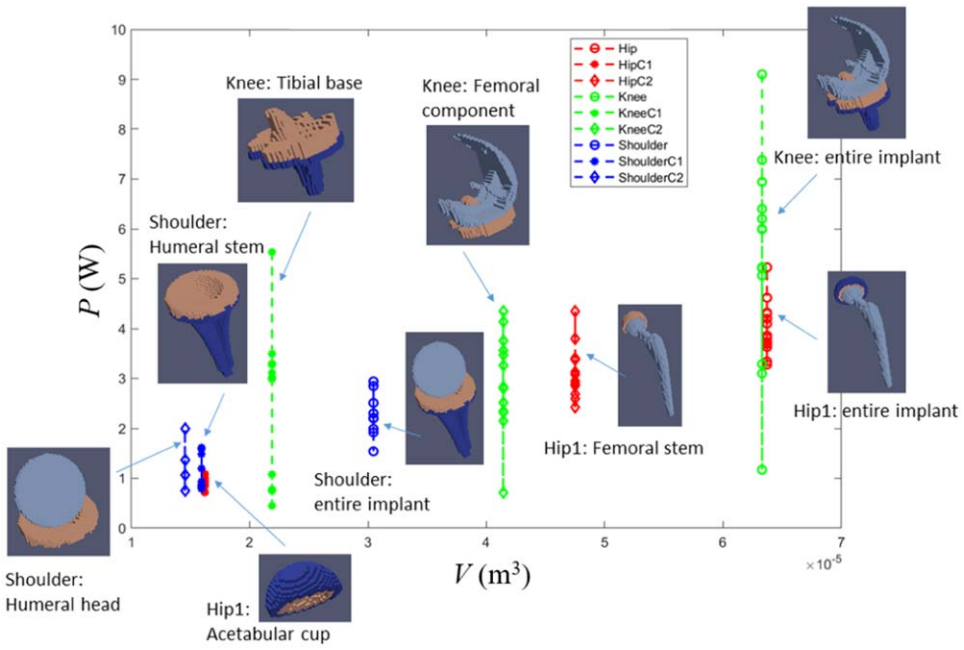

Figure 3. Influence of the GC field orientation on large orthopaedic implants and their components on the deposited power P, plotted against implant volume V. Results for the knee, shoulder and hip1 prostheses are reported here.

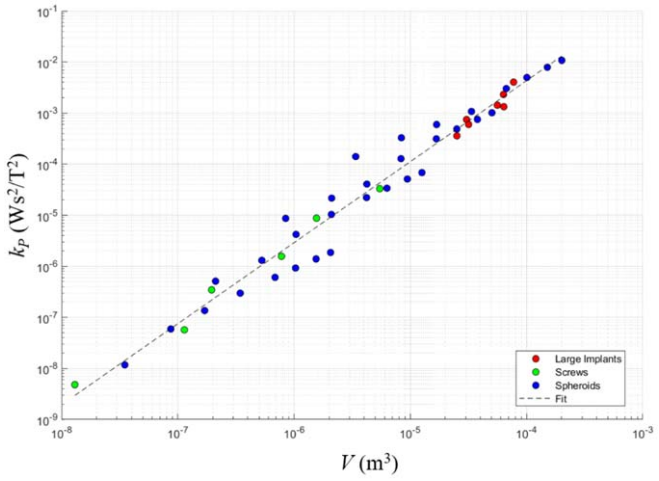

Figure 4. Effect of implant volume V on the k_p coefficients. The results refer to the parametrised objects (spheroids), large orthopaedic implants and screws. For each implant the parameter k_p is plotted, which is related to the maximum power with respect to field orientation.

parameter, defined on a chromatic scale, depends on the aspect ratio (ratio of the maximum and minimum sizes in the xy-plane) and the cross-sectional area S, for several generic plates and for the considered small orthopaedic plates. It is evident that k_p/d increases when increasing the surface area or decreasing the aspect ratio. In particular, a variation of the aspect ratio from 1 to 10 gives rise to a reduction of about one order of magnitude in k_p/d.

3.1.4. Effect of implant conductivity

Implant electrical conductivity directly affects power deposition within the simulations. The total power scales linearly with electrical conductivity until the skin effect starts playing a role within the metallic object, that is until the penetration depth, $\delta = \sqrt{2\rho/\omega\ \mu}$, with ω the angular frequency of the field, ρ the resistivity and μ the permeability of the implant, becomes smaller than the object size. As the harmonic content of the GC signal moves towards high frequencies or the electrical conductivity of the implant increases, the reduction of field penetration determines a sub-linear dependence of the total power with respect to the electrical conductivity.

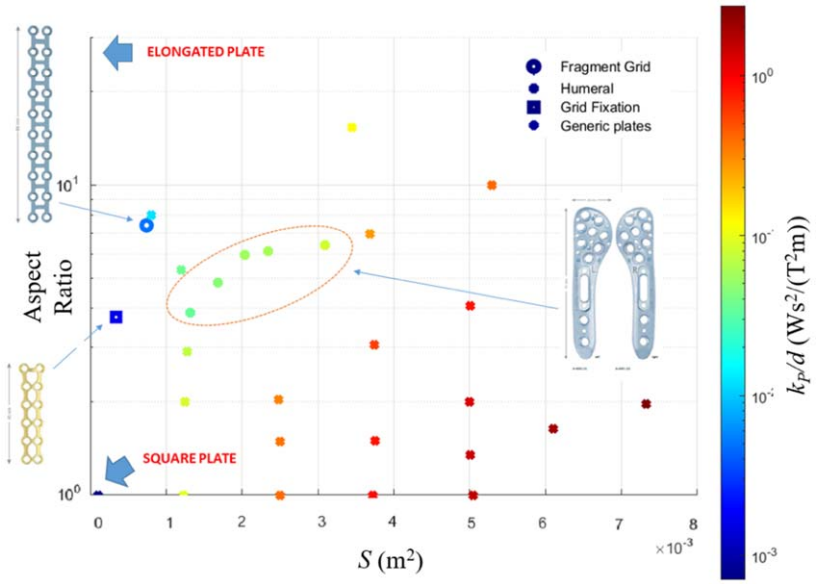

Figure 5. Effect of plate cross-sectional area S and aspect ratio on parameter k_p/d. The results refer to the worst condition of GC field perpendicular to the implant plane ($\alpha = 0°$).

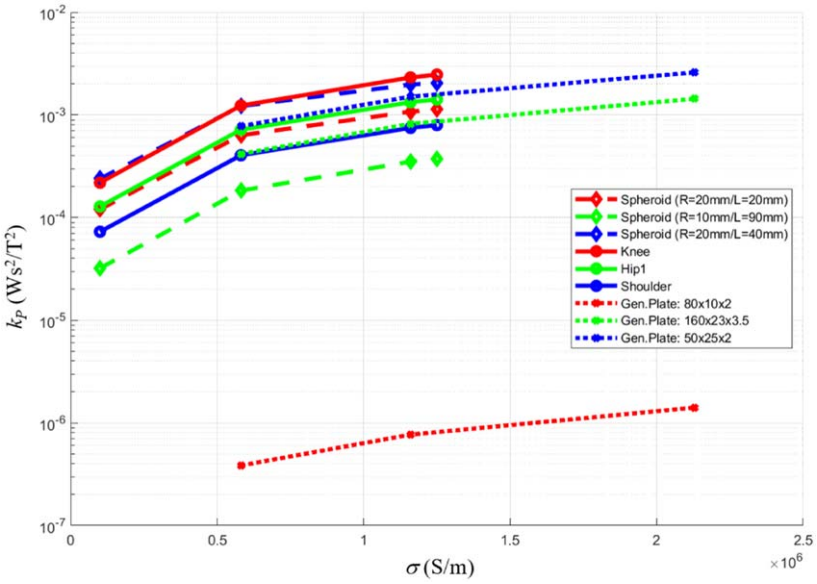

Figure 6. The influence of implant electrical conductivity on coefficient k_p for a selection of large orthopaedic implants, spheroids and generic plates.

Figure 6 shows the coefficient k_p for large orthopaedic implants, a selection of spheroids and a selection of generical plates. The considered range of electrical conductivity covers the metallic alloys most used for orthopaedic implants (CoCrMo-alloy, Ti-alloy, Ti, Steel). The trend is identical for large and small implants.

3.1.5. Effect of phantom properties

The power deposition causes the temperature increase within the implant and the surrounding tissues. For a given object and power deposition, the heating is related to the thermal exchange coefficient of the phantom material, which modifies the heat transfer at the interface between implant and phantom. In order to estimate the function g in equation (7), the maximum temperature rise in large orthopaedic implants was plotted against the ratio of total power P to the external surface of the implant (see figure 7) for three phantom materials (ASTM-gel, bone-type, muscle-type). By linearly fitting the data in the scatter plot related to each phantom

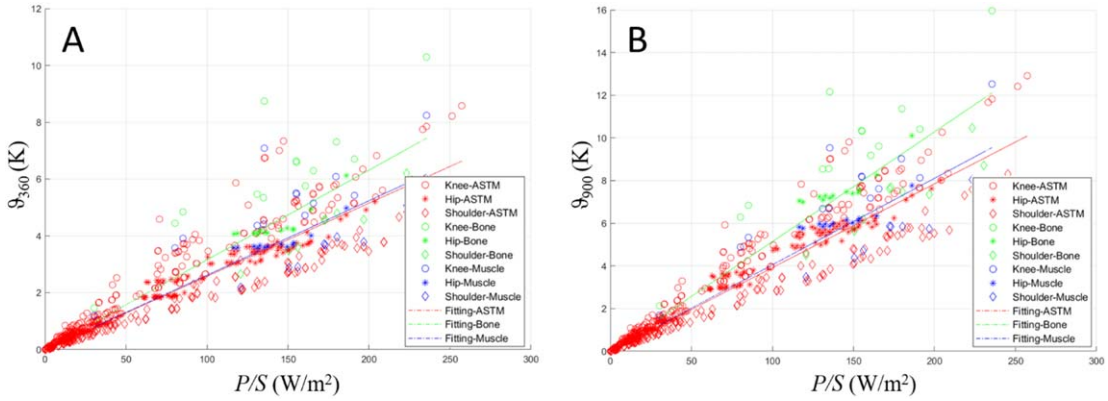

Figure 7. Maximum temperature increase after 360 s (panel A) and after 900 s (panel B) versus the ratio between the total power *P* and the implant external surface area *S*. Colour identifies the phantom material (ASTM gel, muscle or cortical bone), while symbols relate to different implants. Each point relates to a given combination of implant electrical conductivity, sequence and GC field orientation. The curves are the straight-line fits for the set of data corresponding to the same phantom properties.

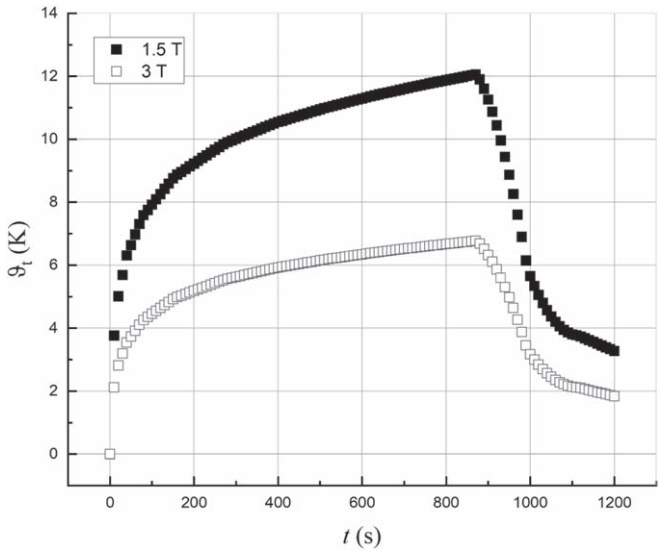

Figure 8. ϑ as a function of time in a 1 mm diameter resonant length Ti-alloy cylinder (176 mm for 1.5 T and 112 mm for 3 T).

property, despite a large dispersion of data being present, a statistically significant correlation of the line slope with the phantom thermal conductivity is found.

3.2. Parameters affecting RF power deposition and heating

As with the GC fields, the RF electromagnetic fields produced by an MRI transmitter coil induce currents within the implant. The heating is caused by associated ohmic losses. However, in this case the heating is maximised in linear conductors, when the induced currents are standing waves formed by reflections at the open ends of the conductor (Dempsey *et al* 2001). In this so-called 'antenna effect', a resonant system is achieved when the length of the conductor is approximately half the wavelength of the RF field within the surrounding medium. In this case, the conductor can be considered as a simple dipole antenna. Even in antennas of negligible thickness, the electrical resonant length is always slightly less than the physical resonant length, such that the reactance is 'tuned out' to present a pure resistance component to the impedance (American Radio Relay League 1949). The resonant length is further reduced in antenna wires of finite thickness (Kozlov and Schaefers 2016); assuming the current within the wire can be approximated by a sinusoid, the resistive and reactive components of the impedance in the wire can be derived using the induced electromotive force (EMF) method (Lee 1984) to calculate a resonant length reduction factor which depends on the diameter of the conductor (appendix C).

The assumption of sinusoidal current distribution breaks down for wires with larger radii or non-cylindrical geometries; in such cases the actual current distribution must be calculated using numerical methods. Approximating solutions such as Pocklinton's or Hallen's Integral equation (Balanis 2005) can be used for such

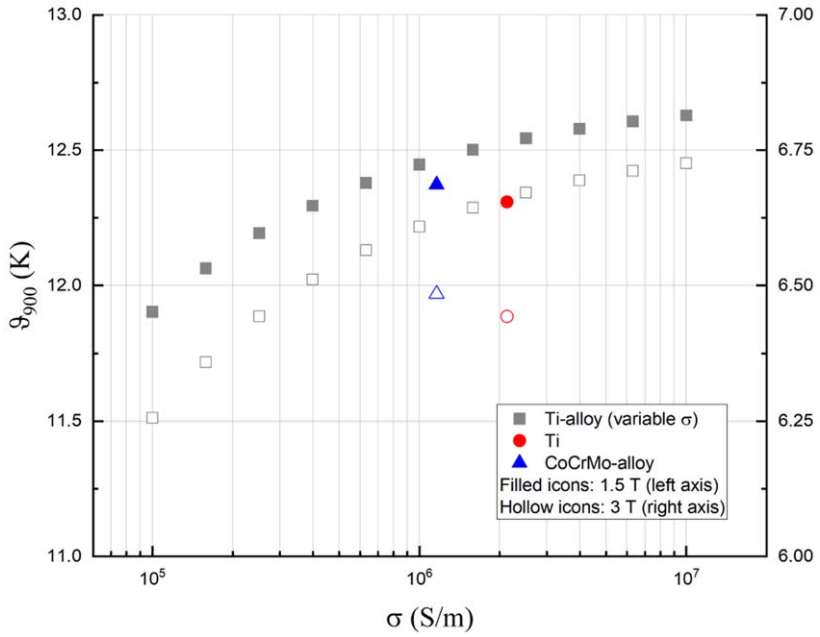

Figure 9. ϑ after 900 s in a 1 mm diameter resonant length Ti-alloy cylinder of variable conductivtiy in ASTM gel.

purposes; however, the general principle remains that the physical resonant length is decreased for devices of larger sizes in the directions perpendicular to resonating current density. Thus, the resonant length of the implant is often empirically stated to sit between one quarter to one half of the RF wavelength. In the sections below, Comsol models were utilised to generate heating data on cylinders, plates and realistic implants. This information is used to investigate the influence of device geometry on implant heating; no attempt has been made at producing numerical approximations to the current density or to calculate the resonant length correction factors directly.

With the time varying magnetic field B_{RF} orientated within the cross-sectional planes of the coil, the antenna effect is largest for linear implants orientated along the coil axis. Similar to the GC heating as set out in equation (6), the heating results can be generalized to any point within the RF coil with a particular incident E field amplitude, and any value of the angle α between the coil axis and implant major length by rescaling the results by a factor $\cos\alpha$. The angle is an important consideration for screw implants, which in typical clinical presentations are placed at right angles to the major bones of the body, and therefore tend to not present any major heating risk. On the contrary, items such as intramedullary nails are orientated within a patient such that the worst-case heating is achieved, although absolute heating is minimised by the larger radii of these devices in comparison to screws (Muranaka *et al* 2007).

The results presented in the sections below represent the maximum temperature increase within the phantom and implant combined geometry. For the cylinders, the maximum temperature is located at the ends of the implant. However for the plates and realistic CAD models, larger temperature rises occur within the phantom (or human tissues *in situ*) compared with the implant, which scatters the electric fields and induces currents within the phantom material (Winter *et al* 2020).

3.2.1. Effect of time

The rate of change of temperature with time is governed by the balance between the absorbed power density from the RF source and the thermal conduction within the phantom material. In a human phantom we would also need to consider the internal metabolic heating and perfusion of blood within vasculated tissues (Guy *et al* 1974). In the initial period the heating rate is almost linear, after which the temperature rise becomes large enough that thermal conduction plays a role in transferring the heat from the implant to the surrounding material. Steady state is achieved once the absorbed power and heat flux to the surrounding medium are equal.

Within the simulations, the RF field is applied for 900 s; then the simulation is continued for a further 300 s with the field switched off. The temperature rise in figure 8 does not tend to zero since the boundary surfaces of the phantom are set with thermal insulation boundary conditions. The temperature prior to 900 s was fitted to a Hill function (Hill 1910) for both B_0 fields. The temperature rise at 360 s and 900 s was 58% and 68% of the steady state value, respectively.

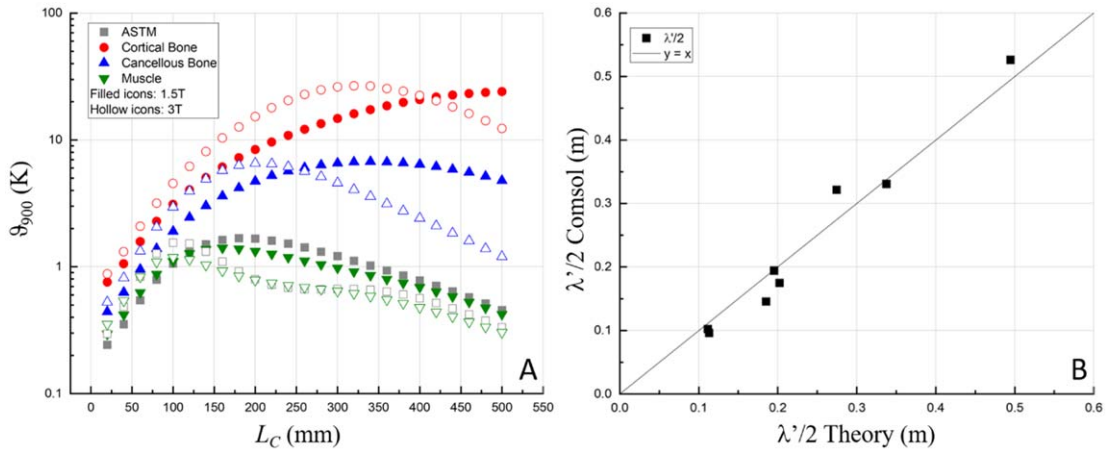

Figure 10. Panel A: Maximum ϑ_{900} due to the presence of 5 mm diameter Ti-alloy rods, in the presence of a local background SAR of 1 W kg^{-1}, in various phantom materials. Panel B: Comparison between the peak centre positions as plotted in the panel A and the theoretical resonant length for a cylindrical dipole antenna.

3.2.2. Effect of implant conductivity

Whilst it is still the case that low electrical conductivity materials result in less Joule heating than is achieved in higher conductivity materials, the absolute value of the σ plays a much more minor role in determining the size of the heating when compared to the GC case. To demonstrate this fact, a 1 mm diameter resonant length cylinder was simulated with variable conductivity in the range 0.1 MS m^{-1} to 10 MS m^{-1}. The observed variation in final temperature over this range is just 6% in the 1.5 T model and 8% in the 3 T model, indicating that differences in heating arising from materials properties is a secondary effect to those observed from changes in the implant geometry.

The thermal properties of the implant are also important to consider. Within figure 9, results are plotted for a resonant length 1 mm cylinders made of pure Ti and CoCrMo-alloy, in both B_0 fields. The electrical condutivity of Ti is nearly twice that of CoCrMo-alloy, however the resultant heating is lower in the former compared with the latter. This is due to the combined effect of the higher values of the heat capacity and thermal conductivity in Ti compared with CoCrMo-alloy (16% and 36% larger respectively). Larger specific heat values serve to increase the energy input required to raise the temperature by a set amount, and the larger thermal conductivity increases the heat flow through the implant and reduces the amplitude of thermal 'hot spots'.

3.2.3. Effect of phantom properties

Within the RF simulations, the electrical properties of the phantom are more important to consider than the thermal properties, since the wavelength of the EM field within the phantom material is the primary factor controlling the antenna effect. The wavelength in a lossy medium (Ulaby 2015) can be written as

$$\lambda = \frac{2\pi}{\omega\sqrt{\frac{\mu\epsilon}{2}\left(1+\sqrt{1+\left(\frac{\sigma}{\omega\epsilon}\right)^2}\right)}}, \tag{8}$$

where ϵ is the medium permittivity, and all other parameters are as previously defined. To illustrate the influence of the EM field wavelength on the antenna effect, a series of simulations were performed on 5 mm diameter Ti-alloy rods of variable lengths situated within phantom materials of various properties (table B2). The calculated temperature rise was normalised to a background local SAR, as calculated by equation (2) at the centre point of the cylinders, of 1 W kg^{-1}. Since the conductivity of both bone types is much lower than that of the ASTM gel or muscle, a much higher applied voltage is required to achieve the same SAR in the phantom. It should also be noted that in order to determine the resonance curve for all tissue types, we have extended the implant size to lengths well beyond those found in real devices. The combination of these factors results in artificially inflated heating that would not exist within clinical scans, requiring the use of a log-scale in panel A of figure 10; however, they have been applied here to ensure equivalence between the simulations.

Panel B shows the general agreement between the simulated resonant lengths in the cylinders extracted from panel A, and the theoretical (reduced half-wavelength) values calculated using the induced EMF method on dipole antennas as set out in appendix C. At a diameter of 5 mm, the assumption of pure sinusoidal current patterns along the length of the cylinders no longer holds and so the scatter in the data in this plot is to be expected.

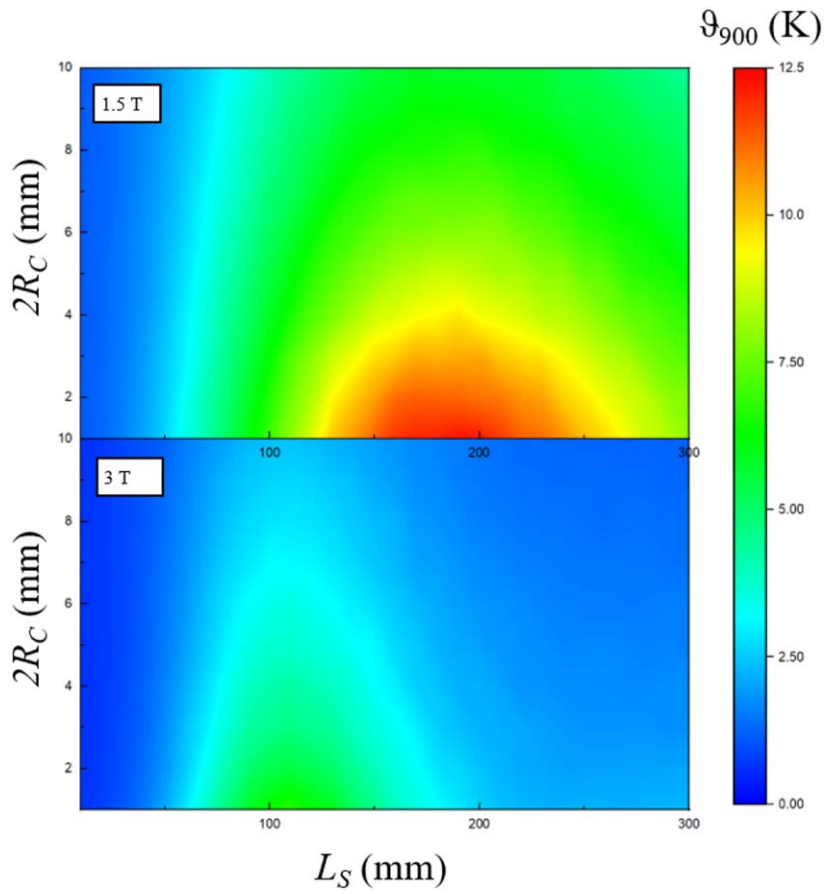

Figure 11. Maximum ϑ_{900} in all Ti-alloy cylinders in ASTM gel as a function of diameter and length in 1.5 T and 3 T.

3.2.4. RF heating: cylinders

Ti-alloy cylinders were simulated within the ASTM phantom, placed 18.5 cm from the central axis of the coil, close to the outer edge of the phantom. Plots of maximum temperatures found in the cylinder models in the range 1 mm to 10 mm diameter and 10 mm to 300 mm length are shown in figure 11 for both 1.5 T and 3 T models. The predominant factor in the implant heating relates to the resonant length, with values of ϑ_{900} decreasing gradually with increasing diameter.

A small amount of noise is visible within the results. The simulations performed to generate panel A of figure 10 utilised a fixed geometry of stacked cylindrical blocks, sequentially changing the materials property of each block to elongate the implant. However this method was too labour-intensive to employ for the large numbers of simulations required for these parametric models, and resulted in finer mesh sizes and therefore longer simulation times. A simple geometrical parametric sweep was therefore used instead; however this method generates a different mesh for each simulation, which results in different mesh discretisation errors. The result is the introduction of a small amount of seemingly random error into the results, but no observable systematic errors.

3.2.5. RF heating: cuboids

Ti-plates were simulated within the ASTM phantom, the centre point placed in the same location for the cylinders, with the normal to the largest surface area along the *y* axis, to replicate an *in vivo* positioning of a plate attached to the outer surface of a bone. Whilst the temperature distribution within the implant is reminiscent of those of a linear conductor, with the maximum increase found at the extremes along the *z* axis, in these plate simulations the azimuthal symmetry as found in the cylinder results is broken; the result is especially pronounced for the wider plates. The temperature rise in one top corner of the plate is found to be larger than that in the equivalent corner on the opposite side of the plate, due to the non-uniformity of the incident E fields (appendix A). The full distribution of maximum temperature rises found in all the plate models (of thickness T_P 1 mm, width W_P 5–25 mm and length L_P 25–250 mm) is shown in figure 12 for both the 1.5 T and 3 T models. Equivalent plots for all the thicknesses (1–3.5 mm) are provided in appendix D.

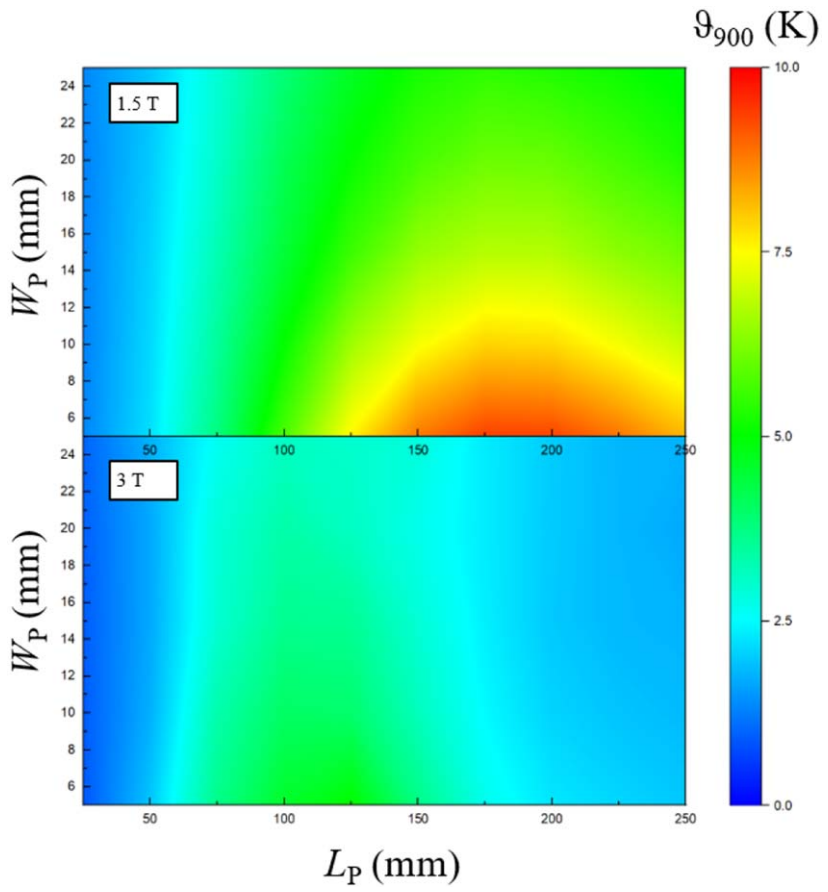

Figure 12. Maximum ϑ_{900} in all 1 mm thick Ti-alloy plate models in ASTM gel as a function of width and length in 1.5 T and 3 T

3.2.6. RF heating: realistic geometries

A series of simulations was carried out on the five humeral and two fixation plates (drawn in the right hand side of figure 1) situated in an ASTM gel phantom. The plates range between 1 mm and 3.4 mm in thickness, 8–13 mm in width and approximately 45–230 mm in length. The plates were situated in the Comsol models with the same position and orientation as the cuboids described above, and the distribution of heating within the implant follows the expected pattern as seen in the simplified geometries, with the largest temperature rise observable at the ends of the plates. Maximum temperatures after 900 s are provided in table 5, and follow the overall pattern of the resonant curves as depicted in figure D1, with a maximum ϑ_{900} found in implant model Humeral 4 (length ~170 mm) in the 1.5 T simulations and in implant model Humeral 2 (length ~115 mm) in the 3 T simulations. The effect of increasing plate thickness is noticeable in the results for the Humeral 1 and Fixation 2 models, which, despite being approximately the same length, show slightly reduced heating in the thicker humeral plates.

4. Discussion

This work has shown that significant heating in orthopaedic implants during MRI scans is possible from exposure to both GC and RF fields. As set out in section 3, there are several factors that affect the power deposition, and the subsequent heating of the implant and phantom. The first factor is simply the size of the applied time-varying field, B_{GC} or B_{RF}. Within the GC simulations, the field gradient is uniform throughout the model with the value 23 mT m^{-1} (an achievable state in MRI coils by design (Domínguez *et al* 2014)) and the amplitude of B_{GC} at the position of the implants is 9.2 mT. The situation within the RF simulations is a little more complex. Whilst the birdcage coil is simulated at the correct resonance to produce the most uniform field over the isocentre plane of the coil (Giovannetti *et al* 2002), in general the field strength varies greatly inside the coil, especially as the implant is moved vertically through the axis of the coil. The field (and field gradient) amplitudes chosen in this study are reasonable representations of clinical situations. Regardless, the heating in both GC and RF simulations will vary with the square of the applied field amplitude.

All the simulations conducted in this work consider the implant immersed in a homogeneous phantom, so possible contributions due to anatomical differences on the RF electromagnetic field distribution and the

Table 3. GC Heating: Comparison between ϑ_{900} in 3D realistic CAD implants, compared with approximating spheroid geometries of similar size. Results shown are for CoCrMo-alloy implants in ASTM gel, with a field angle of 0°, for sequence number 8.

	GC Simulations			
CAD Model	CAD ϑ_{900} (K)	Size (mm)	Spheroid ϑ_{900} (K)	Difference (%)
Hip1	5.57	$R_S = 13.1$ $L_S = 88$	4.97	−11
Hip2	2.05	$R_S = 8.9$ $L_S = 76$	1.69	−18
Hip3	1.67	$R_S = 9.9$ $L_S = 77$	2.27	36
Hip4	8.92	$R_S = 12.1$ $L_S = 92$	4.08	−54
Hip5	17.5	$R_S = 12.6$ $L_S = 116$	4.71	−73
Knee	11.8	$R_S = 16$ $L_S = 59$	7.35	−38
Shoulder	5.52	$R_S = 12.4$ $L_S = 47$	3.77	−32

temperature increase are not analysed. Taking into account the geometrical distribution of the anatomical tissues would significantly increase the number of model parameters, making impossible to obtain general results in a reasonable computational time. It has been shown in the literature that the numerical results are significantly influenced by the tissue distribution within the human model (Fiedler *et al* 2018) and by the body posture (Yang *et al* 2021), suggesting a sensitivity of the models with respect to these parameters.

Total scan time naturally also plays a role in determining final temperature rise. Heat transfer between the implant and the surrounding medium will vary with the thermal material properties and overall surface area of the device, however the ratio of $\vartheta_{360}/\vartheta_{900}$ was found to be approximately 0.76 and 0.92 for the GC and RF simulations respectively. The choice of time sampling was aligned with that in the available measurement standards; however it should be noted that recent advances in coil design and parallel imaging techniques have enabled ultrafast MRI protocols (Peter *et al* 2020, Ahamed *et al* 2020) which may well, in the future, negate many of the risks of implant heating as set out in this study.

A key consideration of heating within the GC simulations is the sequence for switching the gradient fields. As set out in section 3.1.1, the sequences can effectively be described by an index of thermal stress defined in equation (5), proportional to the rate of change of the field switching. A range of clinical sequences was evaluated and compared to simplified, trapezoidal waveforms with frequencies, rise times and peak durations designed to map out the parameter space in which the clinical sequences lie. Figure 2 shows that the deposited power is proportional to the square of the thermal stress index of the sequence for all types of implant. In addition, simulation results of the simplified, trapezoidal sequences matched very closely to the real-world sequences at similar values of I_s, enabling the possibility in the experimental tests to make use of simplifications in modelling techniques whilst achieving essentially the same result. Of all the simulated sequences modelled in this study, SEQ8 produces the highest level of heating due to its high frequency and short rise time as detailed in table 1; the thermal stress index for this sequence is similar to a TrueFisp bSSFP sequence (table 2).

In contrast, the form of the applied field within the RF simulations was modelled as a simple harmonic excitation. In practice, RF sequences in MRI machines generally comprise distinct pulses of sinc-shaped waveforms, followed by (relatively) long pauses. However, previous studies (Wang and Collins 2010) have shown that the whole body normalisation process takes care of any disparities between pulse sequences, with differences only visible on the sub-second level, which is inconsequential within a total scan time of tens of minutes, after which time the same final ϑ_t is reached regardless of the specified RF excitation profile.

Another parameter under investigation was the size and shape of the implants. Whilst the fundamentals of the physics behind GC and RF heating are the same, there remain a number of important differences that drive the results presented in this paper. Volume is noted to be a strong correlate of implant heating from the GC fields (figure 4); however there are many shape configurations which can form a solid of the same volume. As we see in figure 5, worst-case scenarios for GC heating include large surface area plates with the field orientated perpendicular to the face plane so as to maximise the capture area of this effective antenna. Antenna theory is fundamental in understanding the variability of RF heating across the studied geometries and implants. As set

Table 4. GC Heating: Comparison between ϑ_{900} in 2D realistic CAD implants, compared with approximating cuboid geometries of similar size. Results shown are for CoCrMo-alloy implants in bone, with a field angle of 0°, for sequence number 8.

	GC simulations			
CAD model	CAD ϑ_{900} (K)	Size (mm)	Cuboid ϑ_{900} (K)	Difference (%)
Humeral 1	3.76	$L_P = 88$ $W_P = 12$ $T_P = 3$	2.20	-41
Humeral 2	3.83	$L_P = 115.5$ $W_P = 12.5$ $T_P = 3$	2.55	-33
Humeral 3	3.84	$L_P = 142.5$ $W_P = 13$ $T_P = 3$	2.88	-25
Humeral 4	3.63	$L_P = 171$ $W_P = 13$ $T_P = 3.4$		
Humeral 5	4.19	$L_P = 227.5$ $W_P = 12.5$ $T_P = 3.4$	3.01	-28
Fixation 1	0.17	$L_P = 44.1$ $W_P = 8$ $T_P = 1$	0.27	59
Fixation 2	0.29	$L_P = 85$ $W_P = 8.5$ $T_P = 1$	0.37	28

out in section 3.2 and appendix C, with the presence of an in-plane B_{RF} in a birdcage coil, the worst-case heating configurations exist for thin, linear implants orientated with their largest dimension along the coil axis. With this configuration, a resonance of the current flow between the ends of the conductor can be achieved and, as would be expected of a resonance phenomenon, this effect dominates the effects of other parameters that influence implant heating. It is important to note that it is the electromagnetic properties of the phantom material that define the resonant length of the implant (figure 10). In contrast to the GC heating, where increasing the size of the implant results in more heating, with RF heating any deviations in geometry from the worst-case scenario of a resonant length thin wire will result in reduced heating levels.

A series of simplified geometries was studied such that their simulated temperature rises could be compared to the realistic CAD models of implants when the approximate dimensions (and in the case of the GC heating, volumes) are matched. GC heating data for spheroids as a function of size and incident field angle are shown in figure E1. The effect of volume equivalence for heating in this dataset is most clearly evident for the larger incident field angles. Separate plots for spheroid heating data as a function of sequence number and incident field are also provided in figure E2. Here we see similar behaviour for most of the sequences, with the absolute temperature increase dependent on the index of thermal stress parameter as set out in table 1.

The parametric plots for the RF heating in cylinders (figure 11) and cuboids (figure D1) provide evidence for the resonant antenna effect described above. Comparison between the realistic CAD model data and their simplified equivalent geometries are provided in tables 3–5. Dimensions for the spheroids chosen to represent the 3D implants in the GC heating were chosen to maintain the longest length of the implant, but setting the spheroid radius such that the volumes of the two geometries matched. In considering the 2D orthopaedic plates, the major length was replicated in the simplified cuboid geometries, along with the plate thickness. The width was chosen to match the width of the longest section of the implant, especially considering the humeral plates, which become more curved with larger dimensions. Plots of the real and simplified geometries are provided for comparison in figure F1.

Comparison of the data in tables 3–5 show that replacement of complex 3D geometries with simplified shapes can provide a reasonable estimate of the expected heating rise, provided a sensible mechanism is chosen to define the dimensions of the replacement structures. The adoption of a simplified geometry is inappropriate for the 3D implants in the GC simulations (see table 3), which present differences of up to 73% between the 3D implants and the simplified geometries. In the case of the humeral plates, the difference in calculated volume

Table 5. RF Heating: Comparison between ϑ_{900} in 2D Ti-alloy realistic CAD implants, compared with approximating cuboid geometries of similar size. Results shown are for Ti-alloy implants in ASTM gel.

	RF Simulations			
CAD Model	CAD ϑ_{900} (K)	Size (mm)	Cuboid ϑ_{900} (K)	Difference (%)
Humeral 1	1.5 T: 4.69 3 T: 3.54	L_P = 88 W_P = 12 T_P = 3	1.5 T: 4.30 3 T: 3.44	1.5 T: −8 3 T: −3
Humeral 2	1.5 T: 6.18 3 T: 4.20	L_P = 115.5 W_P = 12.5 T_P = 3	1.5 T: 5.61 3 T: 3.46	1.5 T: −9 3 T: −18
Humeral 3	1.5 T: 7.15 3 T: 3.25	L_P = 142.5 W_P = 13 T_P = 3	1.5 T: 6.49 3 T: 3.03	1.5 T: −9 3 T: −7
Humeral4	1.5 T: 7.48 3 T: 2.60	L_P = 171 W_P = 13 T_P = 3.4	1.5 T: 7.27 3 T: 2.53	1.5 T: −3 3 T: −3
Humeral 5	1.5 T: 7.17 3 T: 2.54	L_P = 227.5 W_P = 12.5 T_P = 3.4	1.5 T: 7.35 3 T: 2.59	1.5 T: 2 3 T: 2
Fixation 1	1.5 T: 2.32 3 T: 1.74	L_P = 44.1 W_P = 8 T_P = 1	1.5 T: 2.17 3 T: 1.51	1.5 T: −6 3 T: −14
Fixation 2	1.5 T: 4.86 3 T: 3.87	L_P = 85 W_P = 8.5 T_P = 1	1.5 T: 4.84 3 T: 4.05	1.5 T: −0 3 T: −5

between the simple cuboids and real devices was never more than 11%; however, the same is not true for the fixation plates that have multiple holes in the face. Nonetheless, for the RF simulations presented in table 5, the difference between the real implants and their simplified counterparts was never more than 0.7 K or 17%. The relative differences are larger for the GC heating, with discrepancies between the real implants and the simplified geometries of up to 59%.

Finally materials properties of both the implant and the phantom were investigated. Within both GC and RF simulations, increased electrical conductivity in the implant naturally results in larger induced currents and therefore increased heating. The size of the effect is more pronounced with GC heating than with RF heating. With regards to the phantom materials properties, the heat exchange between the implant and phantom will determine the expected final temperature rise as set out in equation (7). Whether the heating source is the GC or RF field, an increase in phantom thermal conductivity leads to increased thermal flux from the implant to the surrounding tissue and therefore lower heating. As discussed in section 3.2.3, however, within the RF simulations any difference in ϑ due to the phantom thermal properties is secondary to the effect of changing the electrical properties, which define the resonant length of the device. There are two implications of this observation:

(i) The presence of the electrical conductivity in the denominator of equation (8) results in large variations of the resonant length between tissue types (for example, ASTM gel/muscle versus cortical and cancellous bone). It is therefore imperative that the medium surrounding the implant be considered in the experimental design for both simulation and measurement, making the case for simulations in realistic body models over phantoms with average tissue properties. For example, two published studies on intramedullary rods (Muranaka *et al* 2007, Gomez *et al* 2018) came to different conclusions purely from the experimental set up. The first measured the temperature rise in a 1.5 T scanner, using a tissue-equivalent phantom, to be 12.7 °C at a whole-body SAR of 4 W kg^{-1}. As can be inferred from figure 10, the expected temperature rise for the 24 cm implant could be even higher if the phantom had electrical properties closer to that of bone than muscle. However, the second study chose to insert the rods into plastic surgical training bones, with apertures made to enable optical temperature measurements, effectively performing the experiment in air rather than tissue. The dipole half-wavelength in this case increases to 2.4 m and 1.2 m for 1.5 T and 3 T, respectively. Consequently, only a small amount of heating (3.6 °C) was observed in the 3 T measurements and almost no heating ($\leqslant$0.5 °C) in 1.5 T, despite the experiments being carried out at the same whole-body SAR excitation level as in the first study, leading the authors to report that intramedullary rods are safe for use in 1.5 T systems.

(ii) The frequency of the RF field also appears on the denominator of equation (8), bringing the length of smaller implants into the resonant range of heating for high B_0 scanners. Therefore the antenna effect will increasingly become a problem with respect to smaller devices (e.g. orthopaedic screws if orientated along the bore of the magnet, or stents) as higher frequency machines become more prevalent in clinical practice. In these cases, mitigation strategies such as parallel transmission (pTx) systems (Winter *et al* 2020) will be critical in ensuring patient safety.

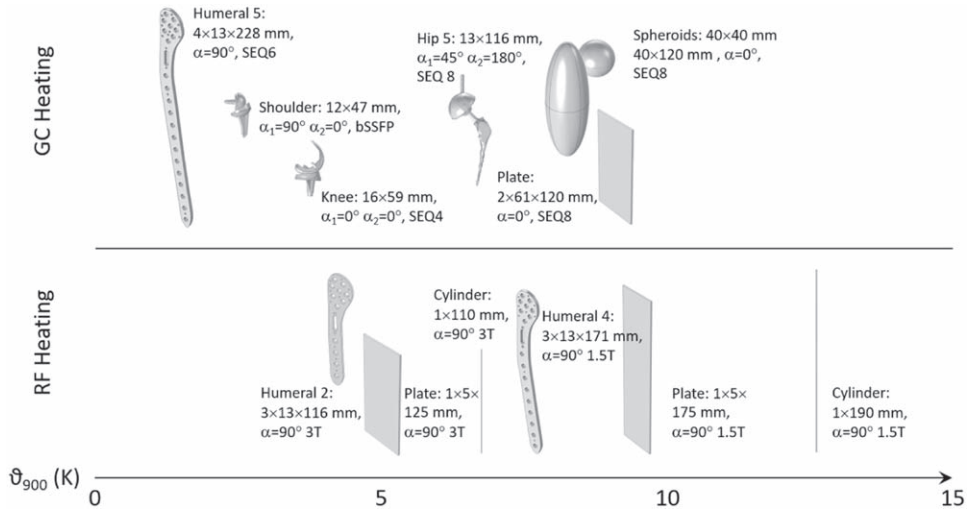

Figure 13. Worst-case configurations of implant geometry, sequence or field strength for each class of implant studied. The heating results presented here are for Ti or Ti-alloy implants situated in ASTM gel. The GC results are scaled for an incident gradient amplitude of 20 mT m^{-1} with the implant situated at 0.25 m from the coil centre, therefore experiencing a B_{GC} amplitude of 5 mT.

5. Conclusion

In this paper we have performed a comprehensive set of simulations to study the expected temperature increase in orthopaedic implants subject to GC and RF fields within MRI scanners. Factors affecting the heating were incorporated into the simulations, to cover the majority of clinical situations that could be expected in the general population of patients with orthopaedic implants, which included:

- GC sequence type
- MRI scan time
- Implant geometry
- Implant electrical conductivity
- Phantom material properties

Worst-case configurations for GC heating include sequences with high-frequency switching and short-pulse rise times, large-volume orthopaedic implants, and large-area plates with the GC field perpendicular to the plate surface. Worst-case configurations for RF heating comprise thin, linear implants of length close to the half-dipole wavelength. With both field types, high-conductivity implant materials lead to higher temperature increases, as do phantom materials with low thermal conductivity, which provide an insulating effect. In general, the factors affecting the implant heating are numerous, and as such are not easily represented in a single framework. Nonetheless, in figure 13 we have summarised the worst-case heating results for each class of implant with respect to the incident GC and RF fields. The results reported in the figure refer to extreme conditions; in clinical scenarios numerous other factors serve to reduce the heating, including the duty cyle, duration of the sequence, orientation of the implant with respect to the field, and position within the coil at distances away from the field 'hot spots'.

Realistic CAD models of implants were compared to models of simplified geometries; the GC simulations included large orthopaedic devices such as hip, knee and shoulder implants, along with a series of two-dimensional bone-fixation plates (the latter were also included in the RF simulations). The results of this study show that in certain cases, simplifications can be made to the models without any major detrimental effects on the simulation results. In particular, full GC sequences can be replaced with simple trapezoidal approximations (in the same way that a simple harmonic excitation is used in the RF simulations in place of the actual RF pulse train). In addition, in some cases, especially for RF simulations, complex geometries can be substituted by simplified shapes, so long as the primary length and overall volume are maintained, yielding the possibility for generic estimates of implant heating for orthopaedic-device manufacturers and simplifying the safety-compliance process. More work is needed to develop parametric models of the effects of implant geometry and other factors presented in this work to investigate the metrological validity of such an approach. Such models should focus on investigation of the factors involved in MRI-

induced heating of the datasets produced in this work, potentially allowing the uncertainty in using results from simplified models or similar devices to be established.

Acknowledgments

This project has received funding from the EMPIR programme co-financed by the Participating States and from the European Union's Horizon 2020 research and innovation programme (grant 17IND01—MIMAS).

Dataset

The final temperature rises for all simulations presented in this paper published as an open access dataset (Wooldridge *et al* 2021).

Appendix A

Within the Comsol simulations, implants were located centrally on the *z* and *x* axes, but offset in *y* so as to be placed within the high-amplitude and high-uniformity region of the E (and therefore SAR) field (shown in the left-hand panels of figure A1). In accordance with ASTM F2182 (ASTM F2182—19e2, 2019) the implants were placed at least 2 cm from the outer wall of the phantom, so as not to perturb the thermal boundary condition at

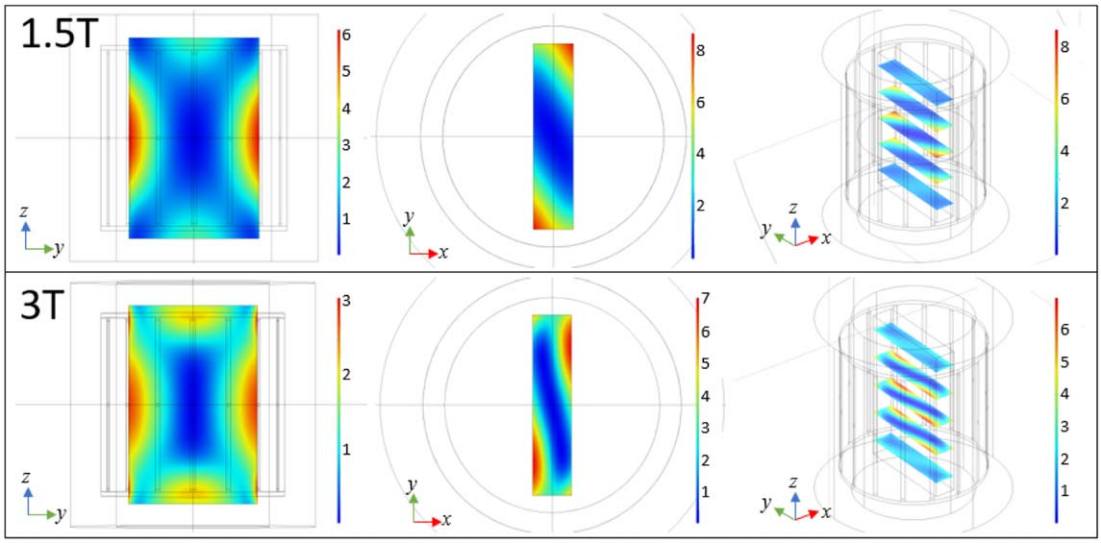

Figure A1. Calculated SAR within the gelled silicon phantom (with no implant, scaled to an average of 2 W kg^{-1} across the whole phantom) at 1.5 T (top row) and 3 T (bottom row). Left panels: the centre longitudinal slice. Centre panels: the isocentre cross-section. Right panels: a series of five evenly spaced cross-sectional plots.

Table A1. Variation of the SAR experienced by linear implants of various lengths positioned within the scanner at a *y* offset of 18.5 cm from the coil centre axis.

Implant length (mm)	SAR variation (%)	
	1.5 T	3 T
25	0.3	0.4
50	1.0	0.8
75	2.0	1.8
100	3.9	3.1
125	5.9	4.7
150	8.6	6.7

that face. Estimates of the SAR uniformity for linear implants of various lengths positioned at this value of y are given in table A1. It should be remembered that for implants of longer length, or implants with significant dimensions in y and/or x, the calculated temperature rise will result from a function of the device geometry, materials properties and also the SAR experienced by the implant within the birdcage coil. For example, the effects of the non-uniform E fields (the right-hand panels of figure A1) can be seen in the asymmetry in the heating on opposite sides of the orthopaedic plates. Whilst the thermal heating results presented in this paper constitute the worst-case scenario for a centrally located ASTM phantom, the actual heating will vary with the relative position of the human or phantom with implant to the coil. For instance, the heating will reduce with non-zero z values (the subject is moved out of the scanner), and will increase if moved in either x or y towards the coils (towards the hotspots visible in the centre panels of figure A1).

Appendix B

The various materials properties of the implant and phantom materials used within this study are presented in tables B1 and B2.

Table B1. The thermal properties of the materials simulated in this study.

Material	Density (kgm^{-3})	Thermal conductivity ($W\ m^{-1}\ K^{-1}$)	Specific heat capacity ($J\ kg^{-1}\ K^{-1}$)
Ti	4512	19.0	523
Ti-alloy	4420	7.2	520
CoCrMo-alloy	8845	14.0	450
ASTM gel	998	0.54	4152
Muscle	1090	0.50	3421
Cancellous bone	1178	0.31	2274
Cortical bone	1908	0.32	1313

Table B2. The electromagnetic properties of the materials simulated in this study.

Material	RF frequency (MHz)	Relative permittivity	Conductivity ($S\ m^{-1}$)
Ti	64 & 128	1	2.13×10^6
Ti-alloy	64 & 128	1	5.81×10^6
CoCrMo-alloy	64 & 128	1	1.16×10^6
ASTM gel	64 & 128	80	0.47
Muscle	64	72.2	0.69
Muscle	128	63.5	0.72
Cancellous bone	64	30.9	0.16
Cancellous bone	128	26.3	0.18
Cortical bone	64	16.7	0.06
Cortical bone	128	14.7	0.07

Appendix C

The cylindrical implants within the RF simulations act as half-wavelength dipoles antennas. In free space, such an antenna has a feed point impedance of 73 Ω in resistance and 43 Ω in reactance, resulting in a slightly inductive reactance. To eliminate this effect, the half wavelength needs to be reduced by a factor R resulting in a net half wavelength of

$$\frac{\lambda'}{2} = \frac{R}{2}\frac{c}{f}, \tag{C.1}$$

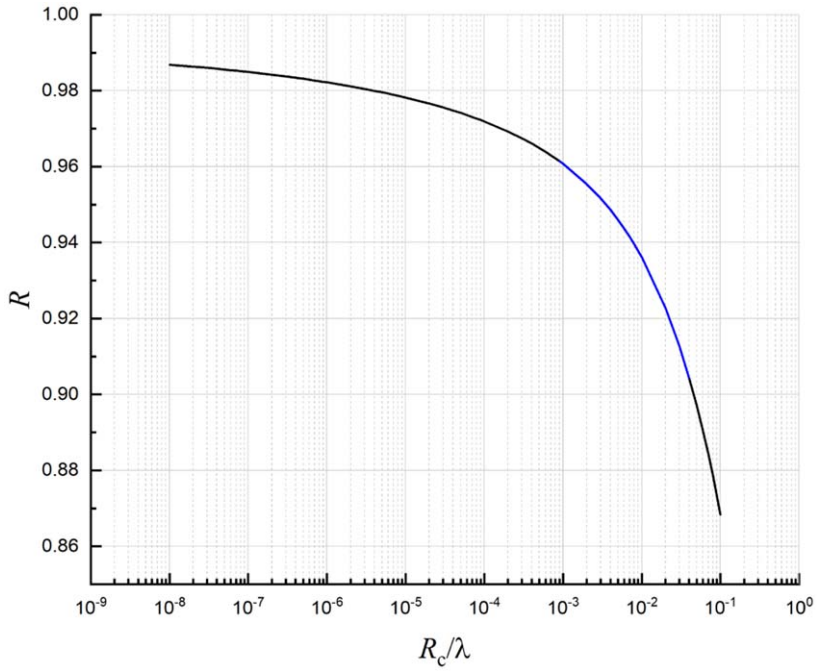

Figure C1. Half-wavelength dipole resonant length reduction factor plotted as a function of the wire radius. The blue highlighted region of the curve represents the region of interest for the geometrical and materials parameters employed in this study.

Table C1. Maximum and minimum R_c/λ for the phantom materials studied.

Material	RF frequency (MHz)	R_c/λ	
		Minimum	Maximum
ASTM gel	64	2.3×10^{-3}	2.3×10^{-2}
	128	4.1×10^{-3}	4.1×10^{-2}
Muscle	64	2.5×10^{-3}	2.5×10^{-2}
	128	4.1×10^{-3}	4.1×10^{-2}
Cancellous bone	64	1.4×10^{-3}	1.4×10^{-2}
	128	2.4×10^{-3}	2.4×10^{-2}
Cortical bone	64	9.6×10^{-4}	9.6×10^{-3}
	128	1.7×10^{-3}	1.7×10^{-2}

where c is the speed of light and f the frequency of the RF signal. The resonance reduction factor R is a function of the dipole antenna wire radius R_c, and can be calculated from the dipole reactance

$$X = \frac{\eta}{2\pi \sin(kL_c/2)}\{\mathrm{Si}(kL_c) + \frac{\cos(kL_c)}{2}[-\mathrm{Si}(2kL_c) + 2\mathrm{Si}(kL_c)] + \frac{\sin(kL_c)}{2}\left[\mathrm{Ci}(2kL_c) - 2\mathrm{Ci}(kL_c) + \mathrm{Ci}\left(\frac{8kR_c^2}{L_c}\right)\right]\}, \quad \text{(C.2)}$$

where η is the impedance of the phantom material, k is the wavenumber, L_c is the cylinder length, and $\mathrm{Si}(x)$ and $\mathrm{Ci}(x)$ are the sine and cosine integral functions. The resonant length $\lambda'/2$ can be found where the reactance vanishes; dividing this length by half the wavelength of the RF field, as calculated in equation (8), provides an estimation of R as a function of the antenna radius.

For each B_0 field and every cylinder diameter studied, there exists a resonant implant length at which the induced currents and therefore heating are maximised. Variations in length for each diameter move the system away from the resonance, resulting in reduced levels of heating. However, it should be noted that the assumption of sinusoidal currents along the length of the cylinder, as required for the validity of equation (C.2), break down for larger radius cylinders, which includes the range of R_c/λ covered in this analysis, as indicated by the blue highlighted section in

figure C1. The exact minimum and maximum ranges for each phantom material and B_0 field are specified in table C1. The same breakdown of sinunsoidal current distrubutions is true for non-cylindrical geometries, and so whilst we expect the analysis above to provide a useful mechanism to understand the physics behind the simulated results, we do not expect a precise match between the simulated and calculated resonant lengths.

Appendix D

Full plots for the cuboid RF models are presented in figure D1, for plates of thicknesses varying from 1 mm to 3.5 mm.

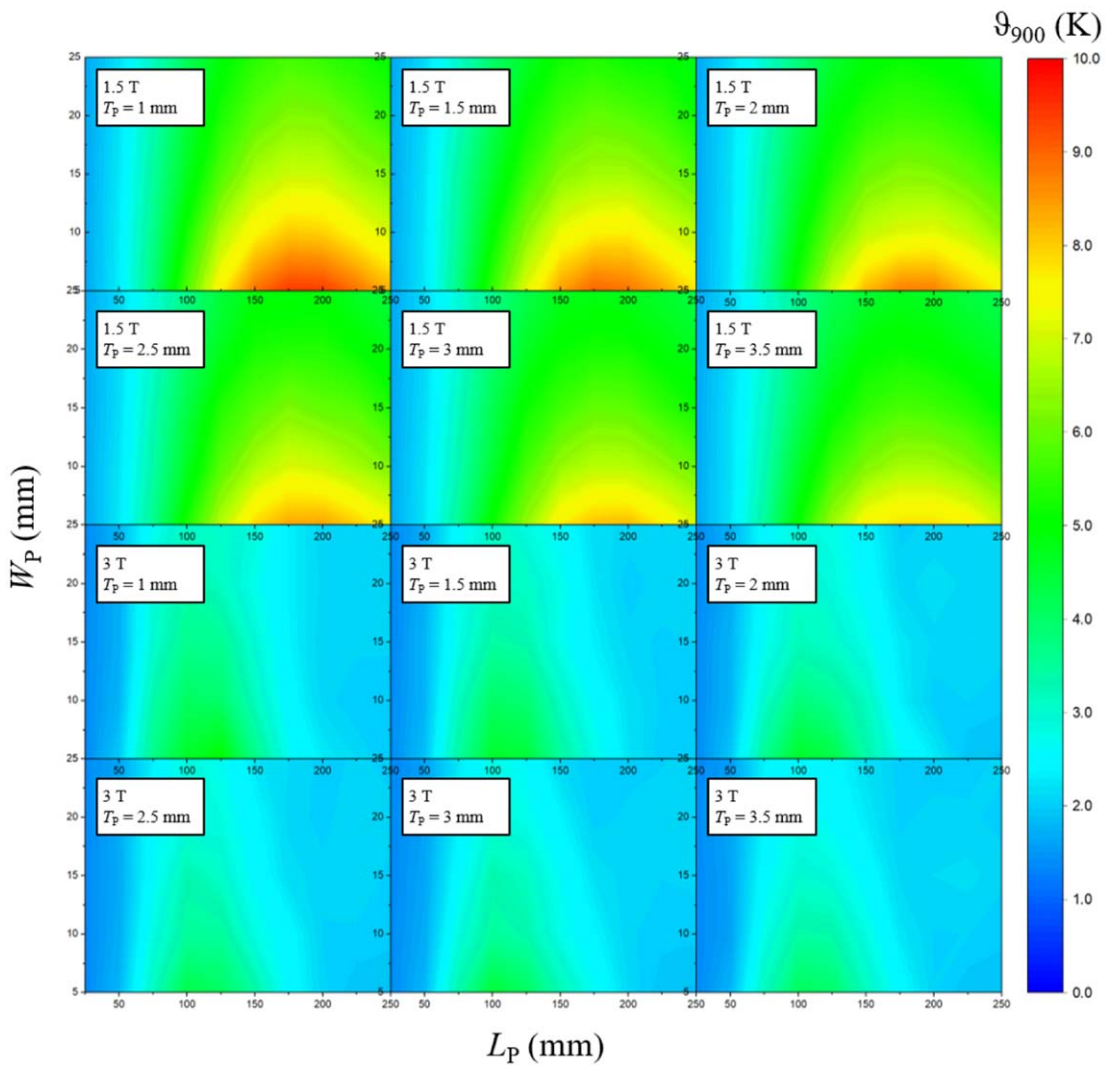

Figure D 1. Maximum ϑ_{900} in all Ti-alloy plates in ASTM gel as a function of width, length and thickness in 1.5 T and 3 T.

Appendix E

Contour plots of GC heating in spheroids are shown in figures E1 and E2.

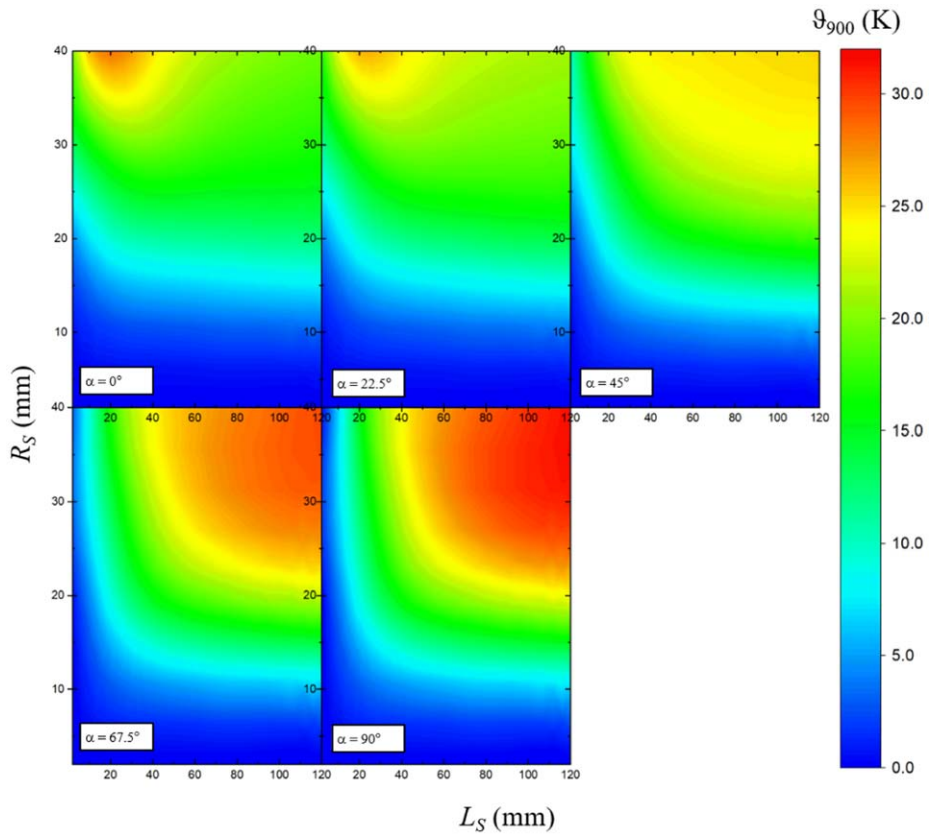

Figure E1. Maximum ϑ_{900} in CoCrMo-alloy prolate spheroid models in ASTM gel as a function of radius R_S, semi-height R_S and incident angle α of the GC field with respect to R_L.

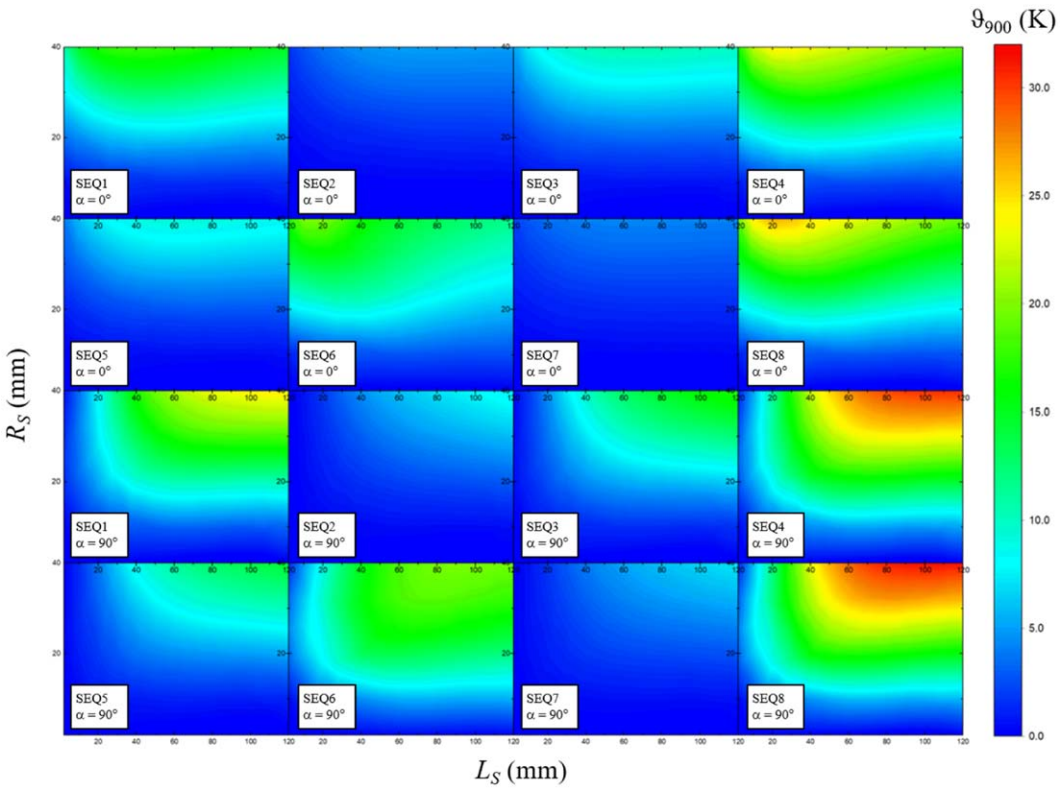

Figure E2. Maximum ϑ_{900} in CoCrMo-alloy prolate spheroid models in ASTM gel as a function of radius R_S, semi-height R_S, incident angle α of the GC field with respect to R_L, and GC sequence number (as described in table 1).

Appendix F

Comparisons of realistic CAD models and their simplified geometry equivalents are shown in figure F1.

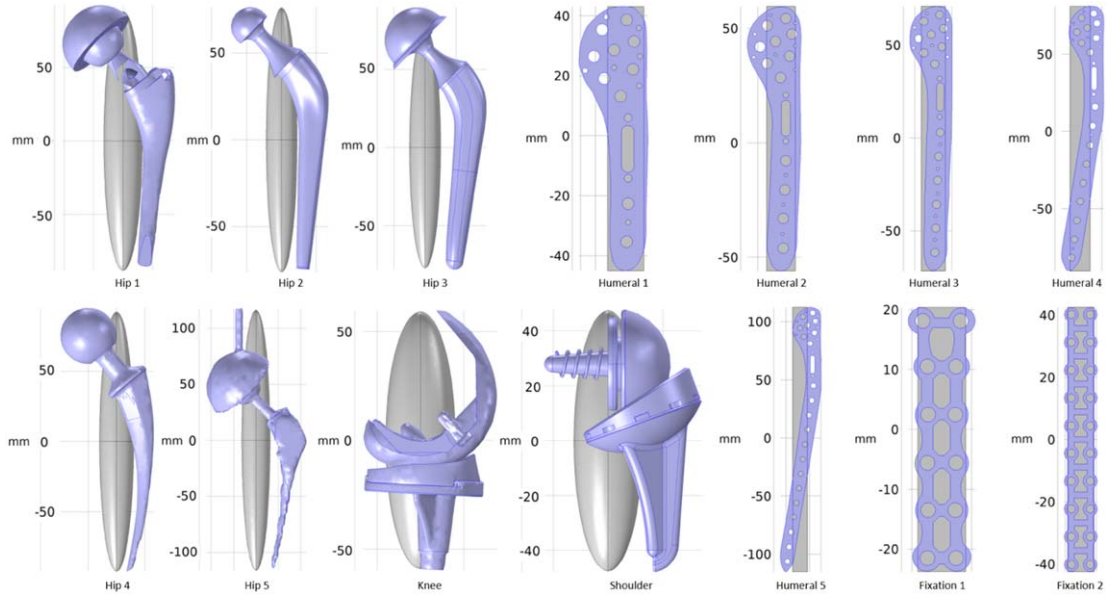

Figure F1. Comparison of the CAD models (in blue) with their simplified geometry equivalents (in grey).

ORCID iDs

J Wooldridge https://orcid.org/0000-0002-9009-1094
A Arduino https://orcid.org/0000-0002-4829-5130
L Zilberti https://orcid.org/0000-0002-2382-4710
U Zanovello https://orcid.org/0000-0001-6415-9967
M Chiampi https://orcid.org/0000-0003-0049-3792
O Bottauscio https://orcid.org/0000-0002-5437-4396

References

Comsol Multiphysics® 2020 v. 5.5. Comsol AB, Stockholm, Sweden (https://comsol.com/)
ASTM F2182—19e2 2019 Standard test method for measurement of radio frequency induced heating on or near passive implants during magnetic resonance imaging.
Ahamed S H, Lee K J and Tang P H 2020 Role of a modified ultrafast MRI brain protocol in clinical paediatric neuroimaging *Clin. Radiol.* **75** 914–20
Arduino A, Bottauscio O, Brühl R, Chiampi M and Zilberti L 2019 In silico evaluation of the thermal stress induced by MRI switched gradient fields in patients with metallic hip implant *Phys. Med. Biol.* **64** 245006
Arduino A, Bottauscio O, Chiampi M and Zilberti L 2017 Douglas-Gunn method applied to dosimetric assessment in magnetic resonance imaging *IEEE Trans. Magn.* **53** 1–4
American Radio Relay League 1949 *The A.R.R.L Antenna Book* V edn (USA: Rumford Press) p 28
Bhuva A N, Moralee R, Moon J C and Manisty C H 2020 Making MRI available for patients with cardiac implantable electronic devices: growing need and barriers to change *Eur. Radiol.* **30** 1378–84
Balanis C A 2005 *Antenna Theory Analysis and Design* III Edition (London: Wiley) pp 443–447
Bottauscio O, Chiampi M, Hand J and Zilberti L 2015 A GPU computational code for eddy-current problems in voxel-based anatomy *IEEE Trans. Magn.* **51** 1–4
Dempsey M F, Condon B and Hadley D M 2001 Investigation of the factors responsible for burns during MRI *J. Magn. Reson. Imaging* **13** 627–31
Domínguez G A, Romero A and Anoardo E 2014 Longitudinal gradient-coil with improved uniformity within the volume of interest *2014 IEEE Biennial Congress of Argentina (ARGENCON) (Bariloche, Argentina, 11–13 June 2014)* (Picastaway, NJ: IEEE) pp 711–5
Fiedler T M, Ladd M E and Bitz A K 2018 SAR simulations & safety *NeuroImage* **168** 33–58
Guy A W, Lehmann J F and Stonebridge J B 1974 Therapeutic applications of electromagnetic power *Proc. IEEE* **62** 55–75
Gomez C, Nelson S, Speirs J and Barnes S 2018 Magnetic intramedullary lengthening nails and MRI compatibility *J. Pediatric Orthopaedics* **38** e584–7
Giovannetti G, Landini L, Santarelli M F and Positano V 2002 A fast and accurate simulator for the design of birdcage coils in MRI *Magn. Reson. Mater. Phys., Biol. Med.* **15** 36–44
Hill A V 1910 The possible effects of the aggregation of the molecules of hmoglobin on its dissociation curves *J. Physiol.* **40** i–vii

ISO/TS 10974:2018 2018 Assessment of the safety of magnetic resonance imaging for patients with an active implantable medical device
Kabil J, Belguerras L, Trattnig S, Pasquier C, Felblinger J and Missoffe A 2016 A review of numerical simulation and analytical modeling for medical devices safety in MRI *Yearbook Med. Inform.* **25** 152–8
Kozlov M and Schaefers G 2016 Influence of lead wire diameter on radio frequency induced power deposition at 64 and 127 MHz *2016 IEEE Conf. on Antenna Measurements Applications (CAMA) (Syracuse, NY,, 23–27 October, 2016)* (Picastaway, NJ: IEEE) pp 1–4
Lidgren L, Raina D B, Tägil M and Tanner K E 2020 Recycling implants: a sustainable solution for musculoskeletal research *Acta Orthopaedica* **91** 125
Lee K F 1984 *Principles of Antenna Theory* (New York: Wiley) pp 29–42
Liu Y, Chen J, Shellock F G and Kainz W 2013 Computational and experimental studies of an orthopedic implant: MRI-related heating at 1.5-T/64-MHz and 3-T/128-MHz *J. Magn. Reson. Imaging* **37** 491–7
Muranaka H, Horiguchi T, Usui S, Ueda Y, Nakamura O and Ikeda F 2007 Dependence of RF heating on SAR and implant position in a 1.5 T MR system *Magn. Reson. Med. Sci.* **6** 199–209
Mosher Z A, Sawyer J R and Kelly D M 2018 MRI safety with orthopedic implants *Orthopedic Clin. North Am.* **49** 455–63
Market Data Forecast 2020 *Europe orthopedic devices market* (https://marketdataforecast.com/market-reports/europe-orthopedic-devices-market)
Peter S C, Wenkel E, Weiland E, Dietzel M, Janka R, Hartmann A, Emons J, Uder M and Ellmann S 2020 Combination of an ultrafast TWIST-VIBE Dixon sequence protocol and diffusion-weighted imaging into an accurate easily applicable classification tool for masses in breast MRI *Eur. Radiol.* **30** 2761–72
Powell J, Papadaki A, Hand J, Hart A and McRobbie D 2012 Numerical simulation of SAR induced around Co Cr Mo hip prostheses *in situ* exposed to RF fields associated with 1.5 and 3 T MRI body coils *Magn. Reson. Med.* **68** 960–8
Ruoff J, Würslin C, Graf H and Schick F 2012 Resolution adapted finite element modeling of radio frequency interactions on conductive resonant structures in mri *Magn. Reson. Med.* **67** 1444–52
Stenschke J, Li D, Thomann M, Schaefers G and W Zylka 2007 A Numerical Investigation of RF Heating Effects on Implants During MRI Compared to Experimental Measurements *Advances in Medical Engineering* (Berlin: Springer) pp 53–8
Schaefers G and Melzer A 2006 Testing methods for MR safety and compatibility of medical devices *Minimally Invasive Ther. Allied Technol.* **15** 71–5
Stijnman P R S, Tokaya J P, Gemert J, Luijten P R, Pluim J P W, Brink W M, Remis R F, Berg C A T and Raaijmakers A J E 2020 Accelerating implant RF safety assessment using a low-rank inverse update method *Magn. Reson. Med.* **83** 1796–809
Ulaby F T 2015 *Antenna Theory Analysis and Design* VII edn (New York: Pearson) ch 7
Winter L, Seifert F, Zilberti L, Murbach M and Ittermann B 2020 MRI-related heating of implants and devices: a review *J. Magn. Reson. Imaging* **53** 1646–65
Wang Z and Collins C M 2010 Effect of RF pulse sequence on temperature elevation for a given time-average SAR *Concepts Magn. Reson.* B **37B** 215–9
Winter L, Silemek B, Petzold J, Pfeiffer H, Hoffmann W, Seifert F and Ittermann B 2020 Parallel transmission medical implant safety testbed: real-time mitigation of RF induced tip heating using time-domain E-field sensors *Magn. Reson. Med.* **84** 3468–84
Wooldridge J, Arduino A, Zilberti L, Zanovello U, Chiampi M and Bottauscio O 2021 Simulations of gradient coil and radiofrequency induced heating of orthopaedic implants in MRI *Zenodo* (https://doi.org/10.5281/zenodo.4926767)
Yang X, Zheng J, Wang Y, Long S A, Kainz W and Chen J 2021 Body-loop related MRI radiofrequency-induced heating hazards: observations, characterizations, and recommendations *Magn. Reson. Med.* **87** 337–48
Zheng J, Lan Q, Zhang X, Kainz W and Chen J 2020a Prediction of MRI RF exposure for implantable plate devices using artificial neural network *IEEE Trans. Electromagn. Compat.* **62** 673–81
Zilberti L, Bottauscio O, Chiampi M, Hand J, Lopez H S, Brühl R and Crozier S 2015 Numerical prediction of temperature elevation induced around metallic hip prostheses by traditional, split, and uniplanar gradient coils *Magn. Reson. Med.* **74** 272–9
Zilberti L, Zanovello U, Arduino A, Bottauscio O and Chiampi M 2020 RF-induced heating of metallic implants simulated as PEC: is there something missing? *Magn. Reson. Med.* **85** 583–6
Zheng J, Ji X, Kainz W and Chen J 2020b Study on search strategies for assessing the worst case RF-induced heating for multi-configuration implant system under MRI *IEEE Trans. Electromagn. Compat.* **62** 43–51
Zheng J, Lan Q, Kainz W, Long S A and Chen J 2020 Genetic algorithm search for the worst-case MRI RF exposure for a multiconfiguration implantable fixation system modeled using artificial neural networks *Magn. Reson. Med.* **84** 2754–64